Supplementary Information

Structural insight into the intraflagellar transport complex IFT-A and its assembly in the anterograde IFT train

Yuanyuan Ma[1,2#], Jun He[1,2#], Shaobai Li[1,2], Deqiang Yao[3], Chenhui Huang[1,2], Jian Wu[1,2*] and Ming Lei[1,2,4*]

[1]Ninth People's Hospital, Shanghai Jiao Tong University School of Medicine, Shanghai 200011, China.

[2]Shanghai Institute of Precision Medicine, Shanghai 200125, China.

[3]Renji Hospital, Shanghai Jiao Tong University School of Medicine, Shanghai 200032, China.

[4]State Key Laboratory of Oncogenes and Related Genes, Shanghai Jiao Tong University School of Medicine, Shanghai 200025, China.

[#]These authors contributed equally to this work.

*Correspondence: M.L. (leim@shsmu.edu.cn) and J.W. (wujian@shsmu.edu.cn)

Supplementary Fig. 1

a

Protein name	Uniprot Accession Number	MW(kDa)	Peptide spectrum matches	Unique peptides
IFT121	Q22U89	137.8	145	74
IFT139	I7MFN3	153.9	116	67
IFT144	Q22BP2	158.1	114	65
IFT140	I7LVZ7	161.4	101	55
IFT122	Q244W3	143.7	86	55
IFT43	Q22NF5	16.7	3	3

b

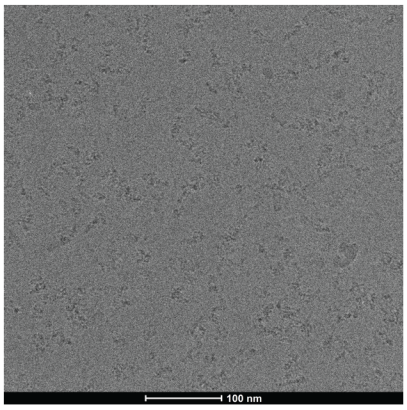

Supplementary Fig. 1 | Biochemical and cryo-EM analyses of the purified IFT-A complex. a, Mass spectrometry analysis of the purified IFT-A complex. **b,** A representative cryo-EM image of IFT-A. Each experiment was repeated three times independently with similar results. Source data are provided as a Source Data file.

Supplementary Fig. 2

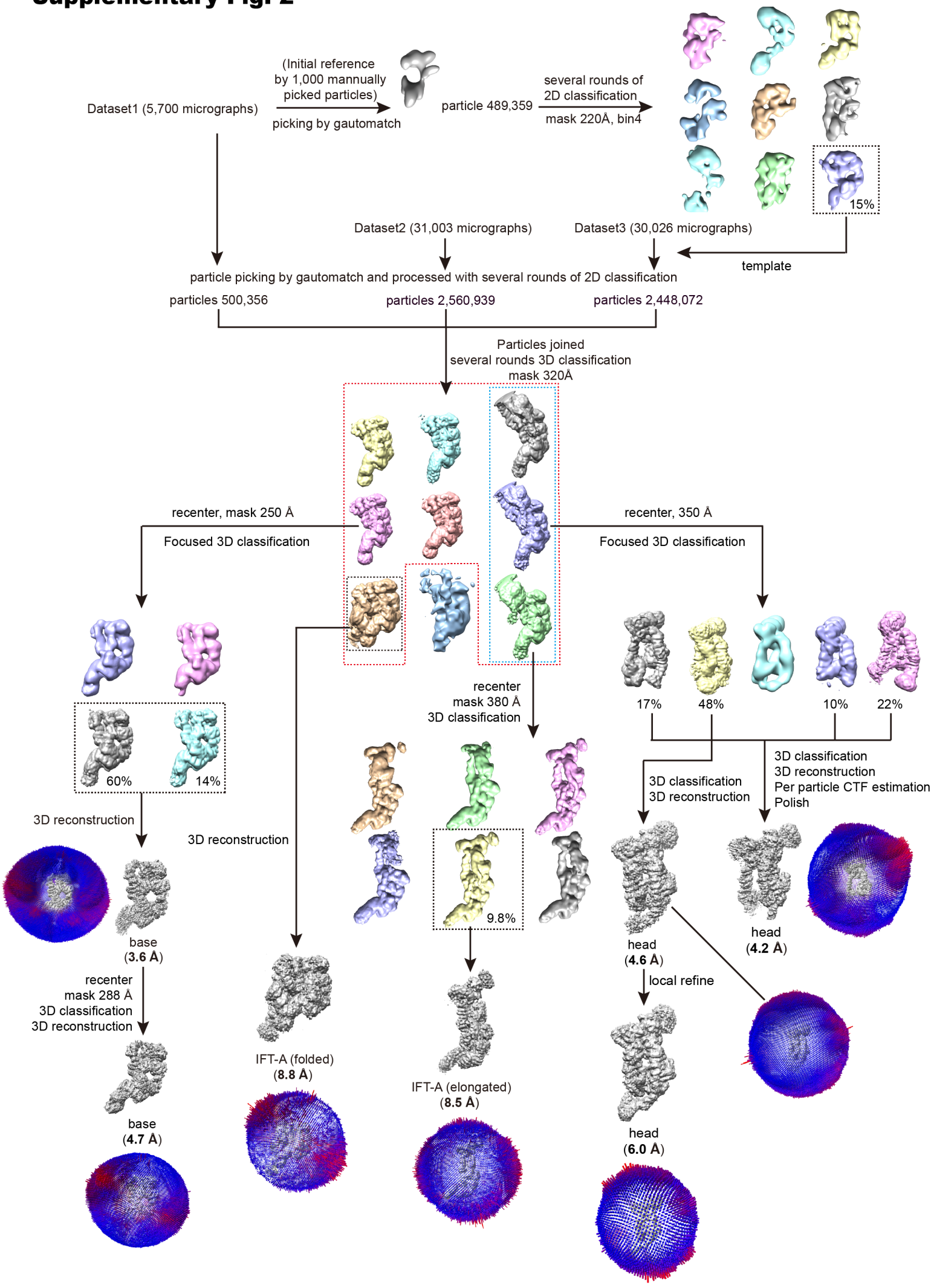

Supplementary Fig. 2 | Structure determination of the IFT-A complex by cryo-EM. Cryo-Image processing flowchart, reconstruction of the IFT-A complex and angular distribution of reconstructed particles.

Supplementary Fig. 3

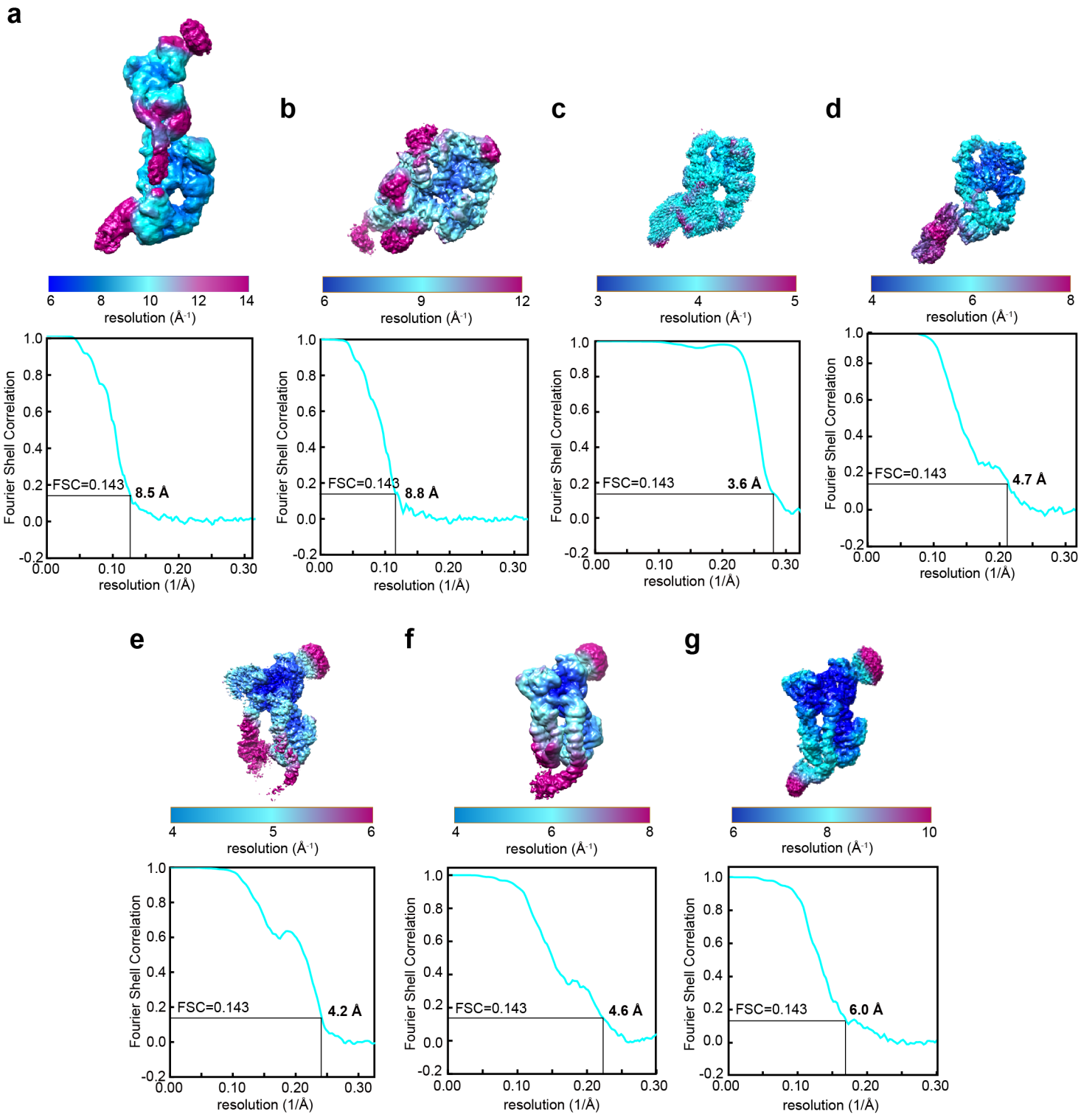

Supplementary Fig. 3 | Local resolution estimation of IFT-A. a-g, Local resolution maps and the corresponding Fourier Shell Correlation curves for IFT-A in elongated state (a), IFT-A in folded state (b), base module at 3.6 Å (c), base module at 4.7 Å (d), head module at 4.2 Å (e), head module at 4.6 Å (f) and head module at 6.0 Å (g).

Supplementary Fig. 4

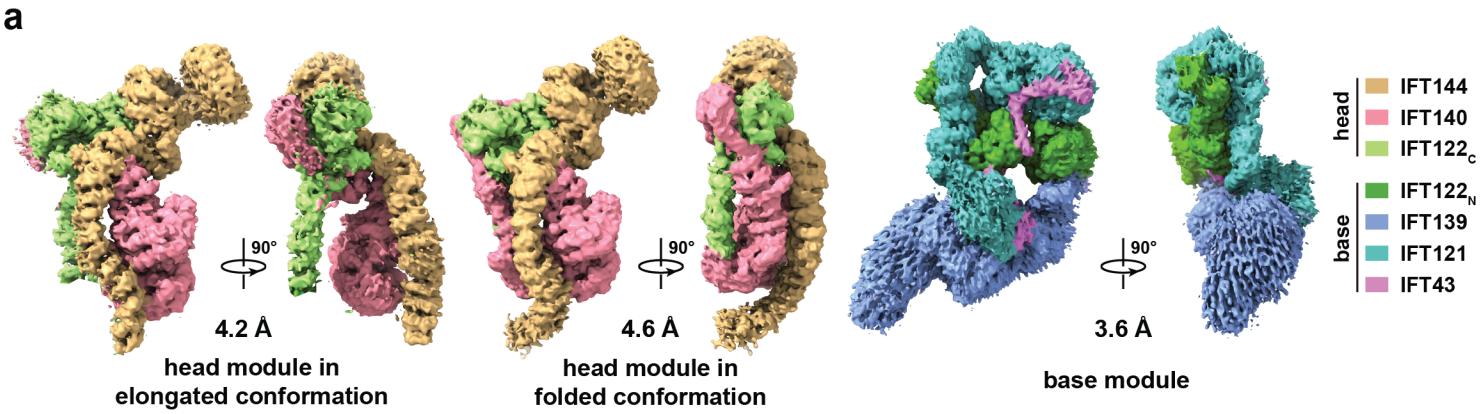

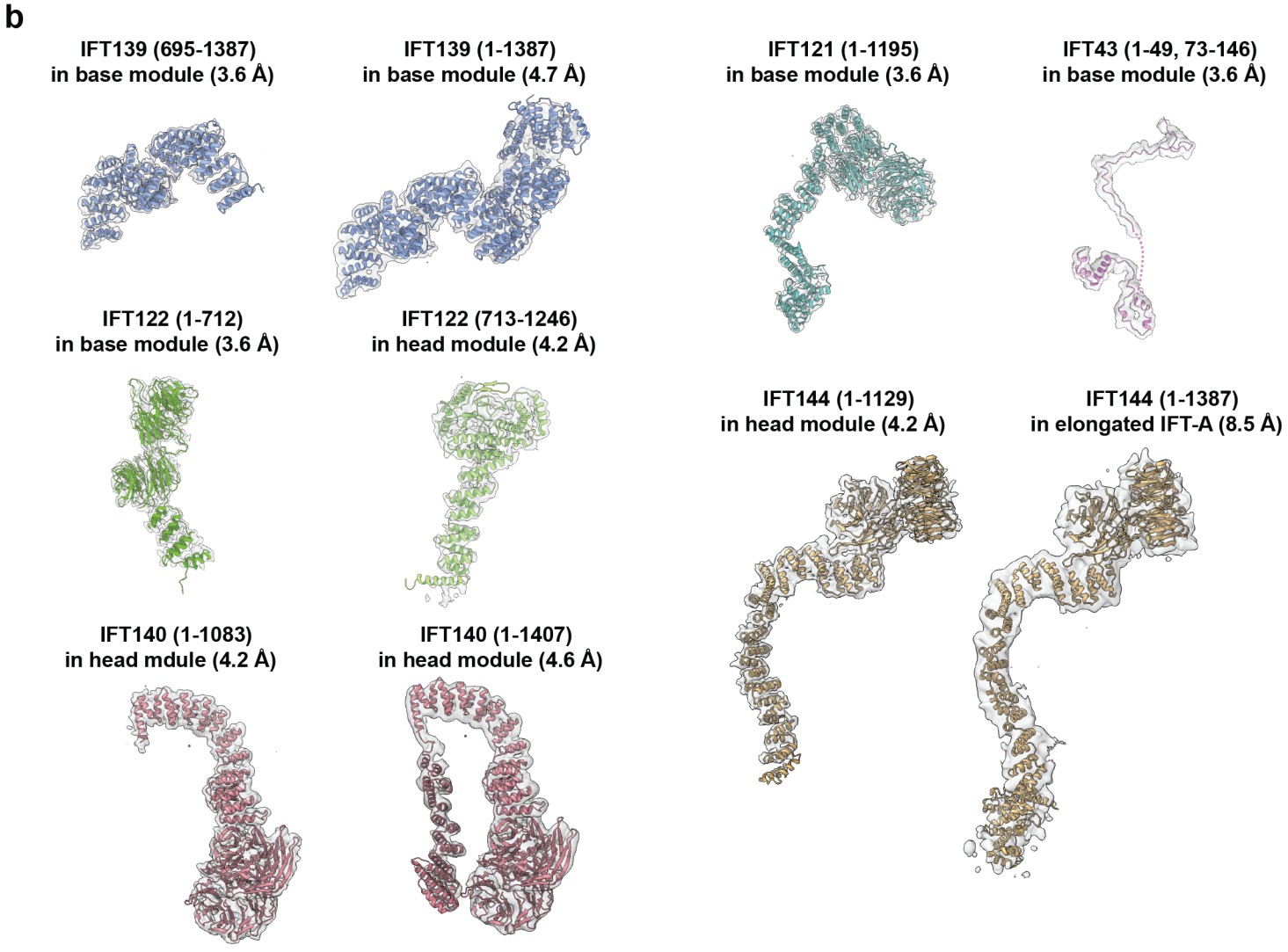

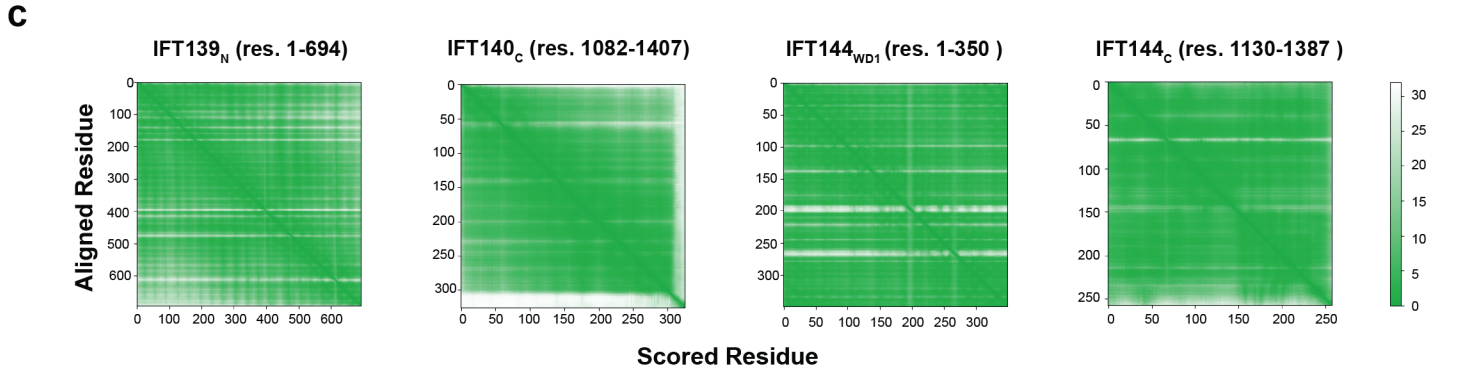

Supplementary Fig. 4 | Cryo-EM density maps of the IFT-A complex. a, High-resolution density maps of the head and base modules in two orthogonal views. The IFT-A components are colored and the color scheme is shown on the right. **b,** Cryo-EM density maps of the IFT-A subunits with the atomic models in cartoon representation. **c,** Predicted aligned error (PAE) plots of AlphaFold-2 predicted $IFT139_{N}$, $IFT140_{C}$, $IFT144_{WD1}$ and $IFT144_{C}$.

Supplementary Fig. 5

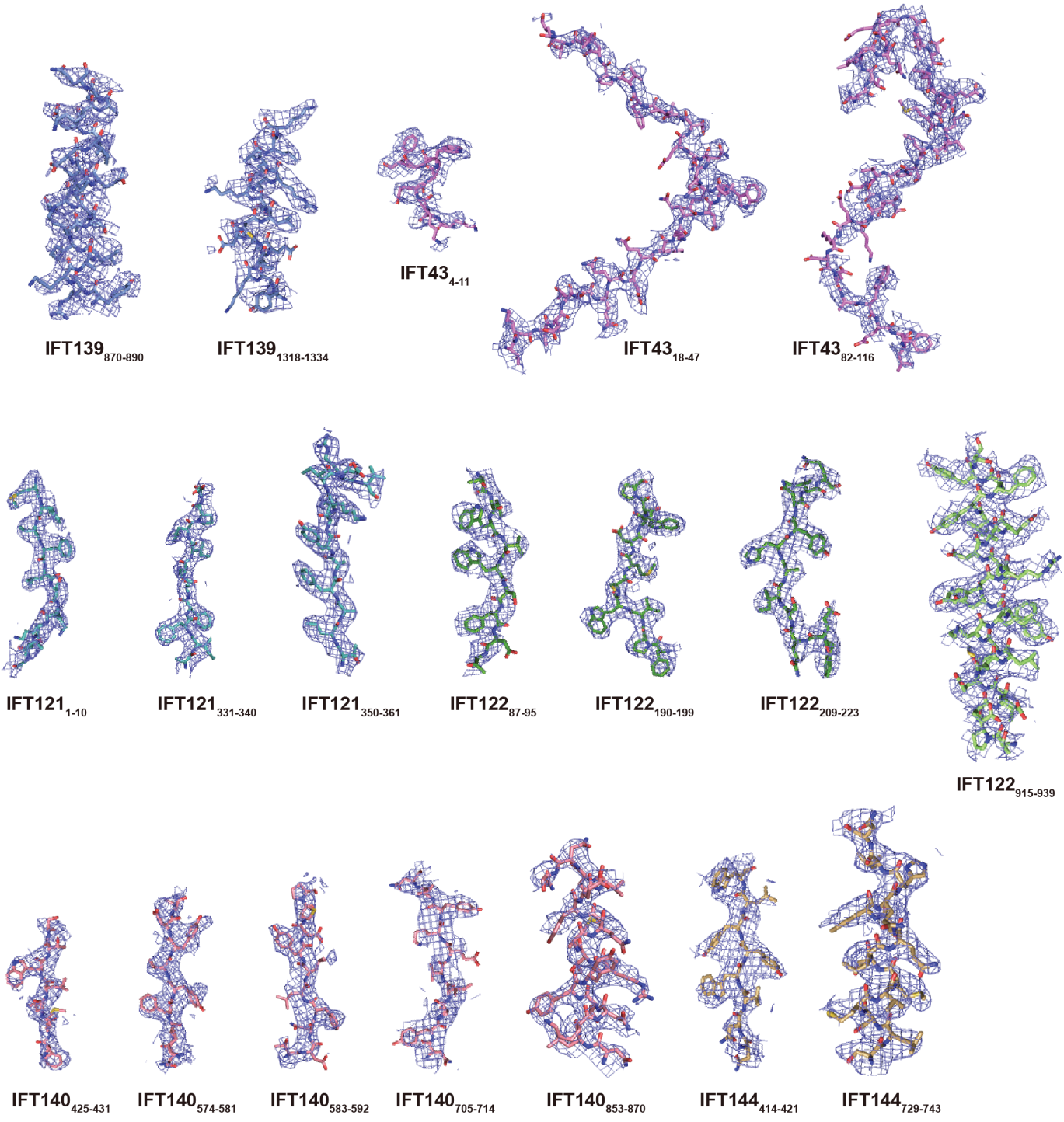

Supplementary Fig. 5 | Representative cryo-EM density maps for the selected elements of each component of IFT-A.

Supplementary Fig. 6

Supplementary Fig. 6

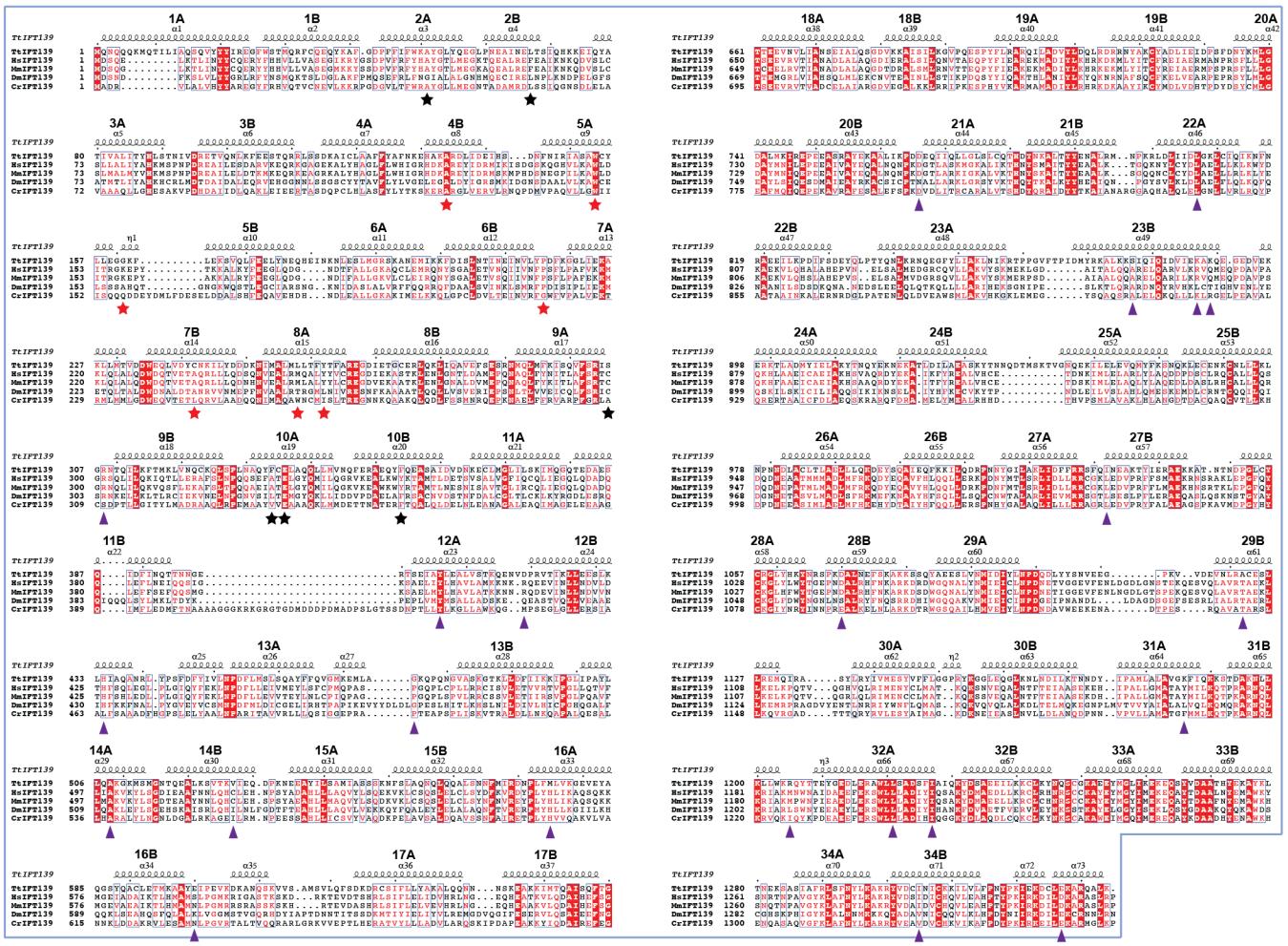

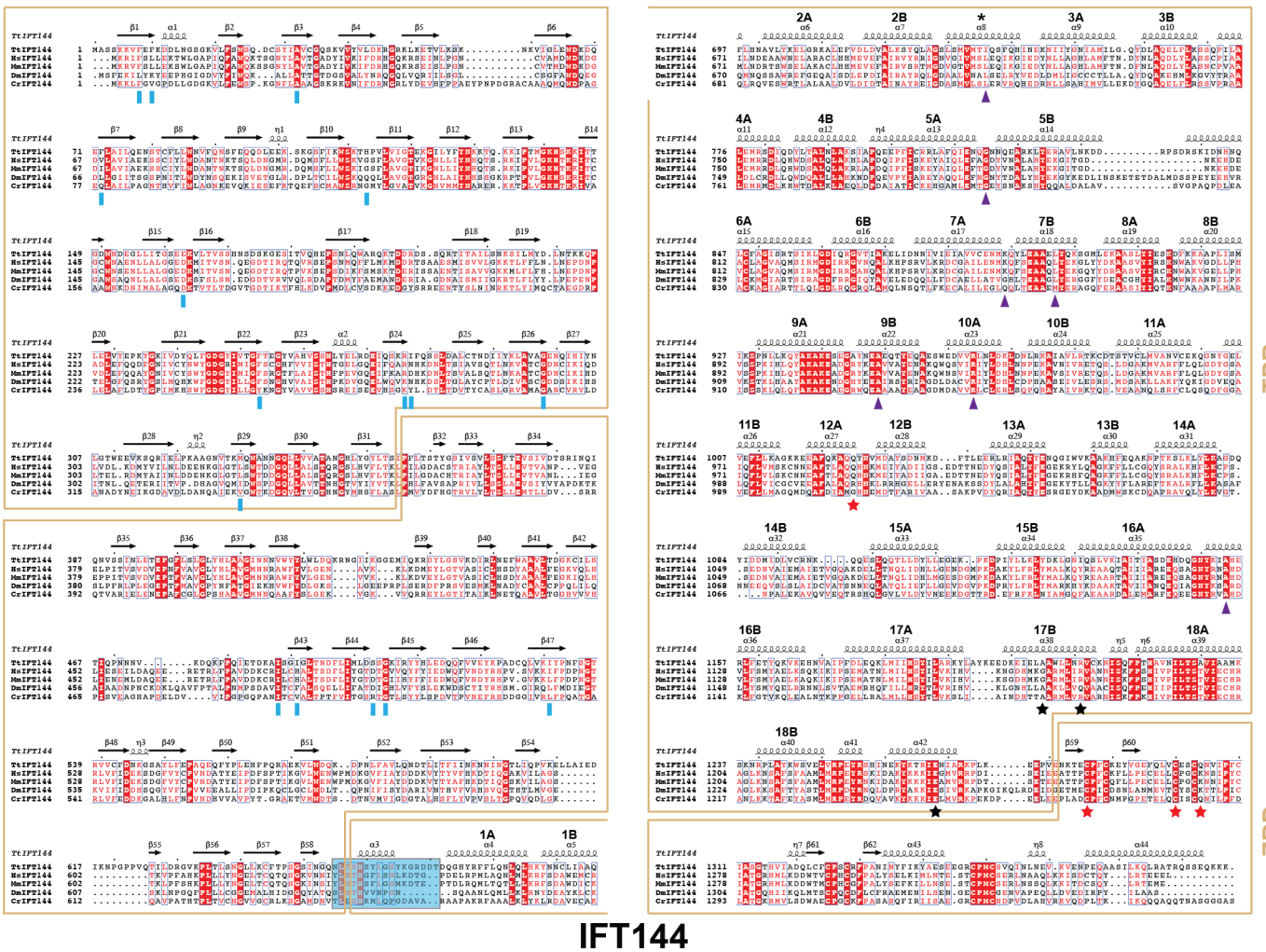

Supplementary Fig. 6

Supplementary Fig. 6 | Multiple sequence alignment of the IFT-A components. a-f, Sequences of several representative organisms are used for alignment in IFT121 (**a**), IFT122 (**b**), IFT139 (**c**), IFT144 (**d**), IFT140 (**e**) and IFT43 (**f**). The short names Tt, Hs, Mm, Dm and Cr are the abbreviations of *Tetrahymena thermophila*, *Homo sapiens*, *Mus musculus*, *Drosophila melanogaster* and *Chlamydomonas reinhardtii*, respectively. **a,** Accession numbers used for IFT121 are as follows: Q22U89 (Tt), Q9P2L0 (Hs), Q8BND3 (Mm), Q9W097 (Dm) and A8JFR3 (Cr). **b,** Accession numbers used for IFT122 are as follows: Q244W3 (Tt), Q9HBG6 (Hs), Q6NWV3 (Mm), Q9VSJ6 (Dm) and H9CTG6 (Cr). **c,** Accession numbers used for IFT139 are as follows: I7MFN3 (Tt), Q7Z4L5 (Hs), Q0HA38 (Mm), A0A0Q9X6X6 (Dm) and A9XPA6 (Cr). **d,** Accession numbers used for IFT144 are as follows: Q22BP2 (Tt), Q8NEZ3 (Hs), Q3UGF1 (Mm), A1ZBM3 (Dm) and A9XPA7 (Cr). **e,** Accession numbers used for IFT140 are as follows: I7LVZ7 (Tt), Q96RY7 (Hs), E9PY46 (Mm), Q7KTZ4 (Dm) and Q68K27 (Cr). **f,** Accession numbers used for IFT43 are as follows: Q22NF5 (Tt), Q96FT9 (Hs), Q9DA69 (Mm), Q9VK67 (Dm) and A8HYP5 (Cr). The two helices in each TPR motif are distinguished and labeled as helix A and B. Linkers between the WD and TPR domains of IFT122, IFT121, IFT144, IFT140 are highlighted in light blue shadows. The Loop-45 in IFT122 crucial for formation of the elongated and folded IFT-A complexes is highlighted with a cyan rectangle. Mutations that impair cargo binding, interactions of the components within IFT-A, interactions between IFT-As, or interactions between IFT-A and IFT-B are denoted by blue rectangles, purple triangles, red stars and black stars under the sequences, respectively.

Supplementary Fig. 7

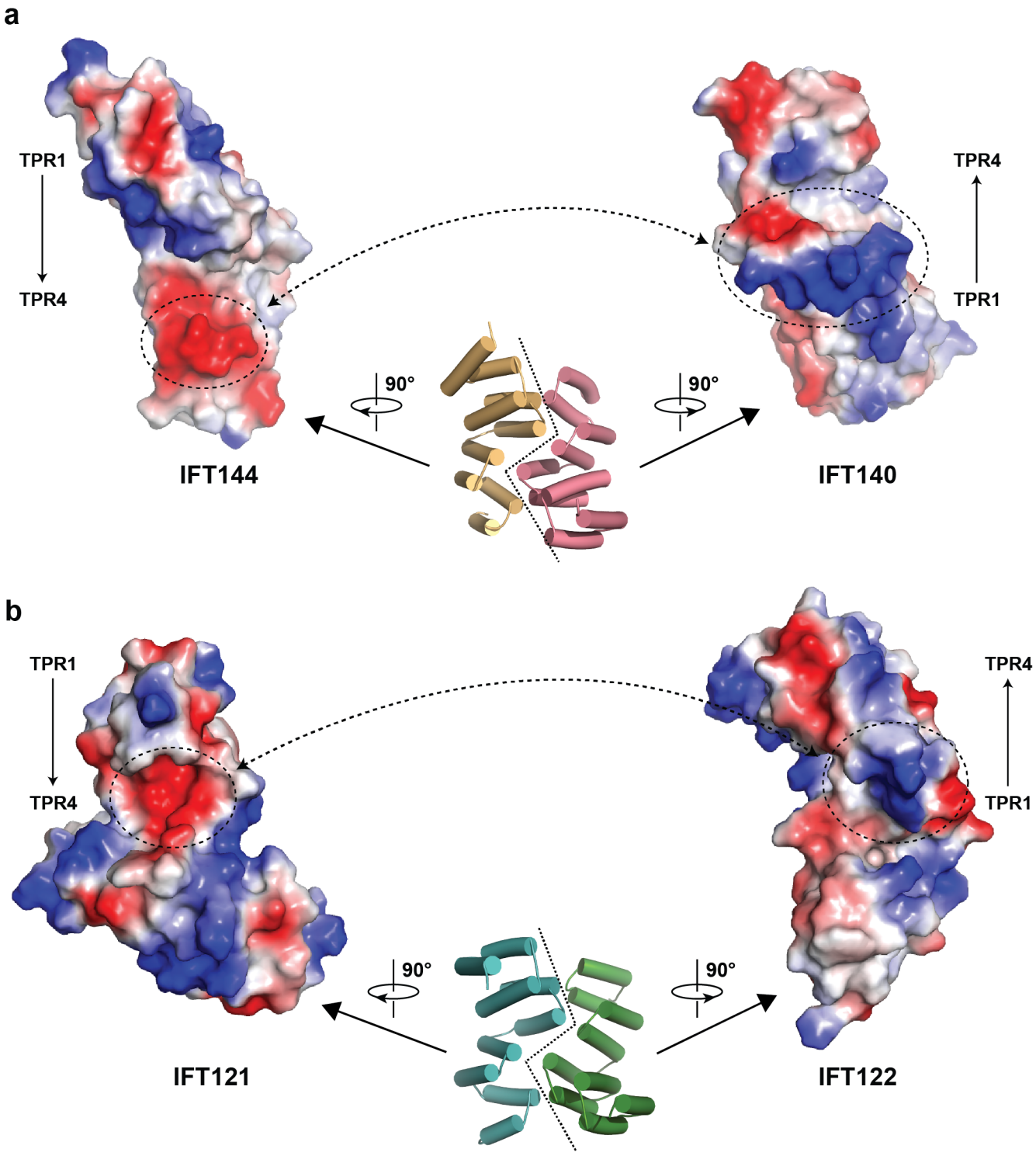

Supplementary Fig. 7 | Electrostatic surface potential showing the interactions at the TPR junctions. The opposite electrostatic surfaces important for the IFT144-IFT140 interaction **(a)** and the IFT122-IFT121 interaction **(b)** are highlighted in dashed circles. Positive potential, blue; negative potential, red.

Supplementary Fig. 8

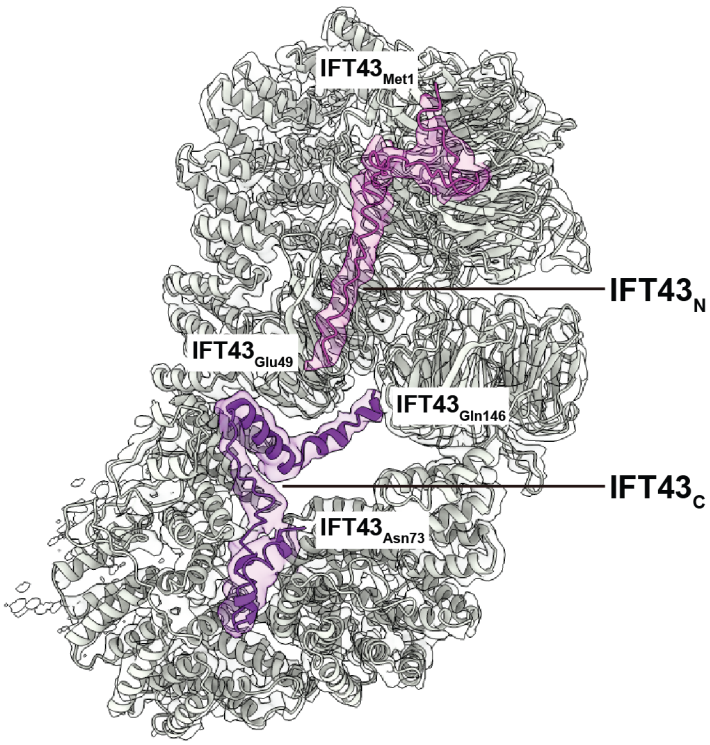

Supplementary Fig. 8 | IFT43 in the base module. Atomic models of $IFT43_N$ and $IFT43_C$ are colored in violet and purple respectively, while other IFT-A components and the density map of the base module in grey.

Supplementary Fig. 9

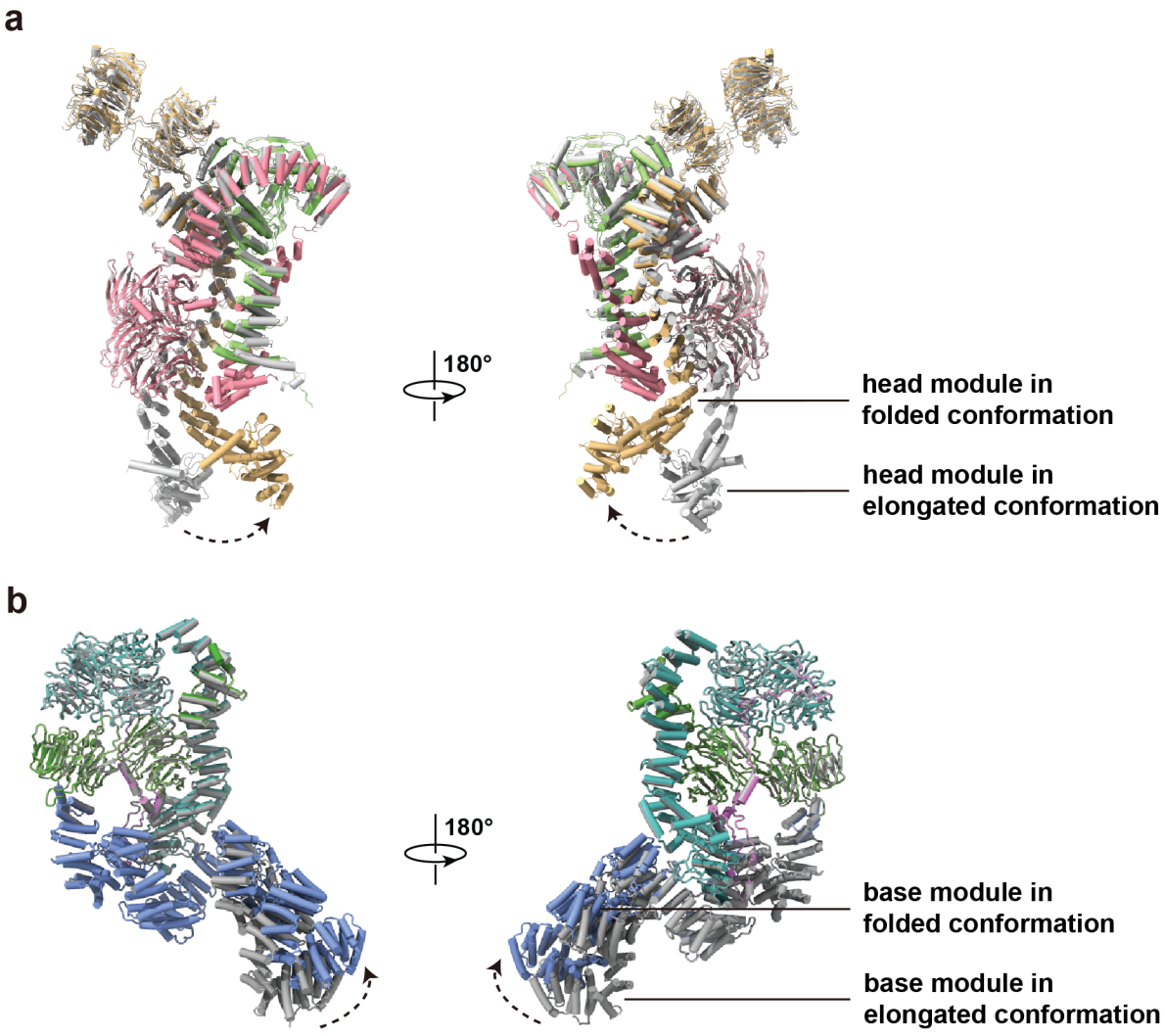

Supplementary Fig. 9 | Structural alignment of the head and base modules. a-b, Two opposite views of the head **(a)** and base **(b)** modules. Proteins in the folded state are colored as Fig. 1a, and those in the elongated state in gray. The black arrows indicate the flex of $IFT144_C$ and $IFT139_N$.

Supplementary Fig. 10

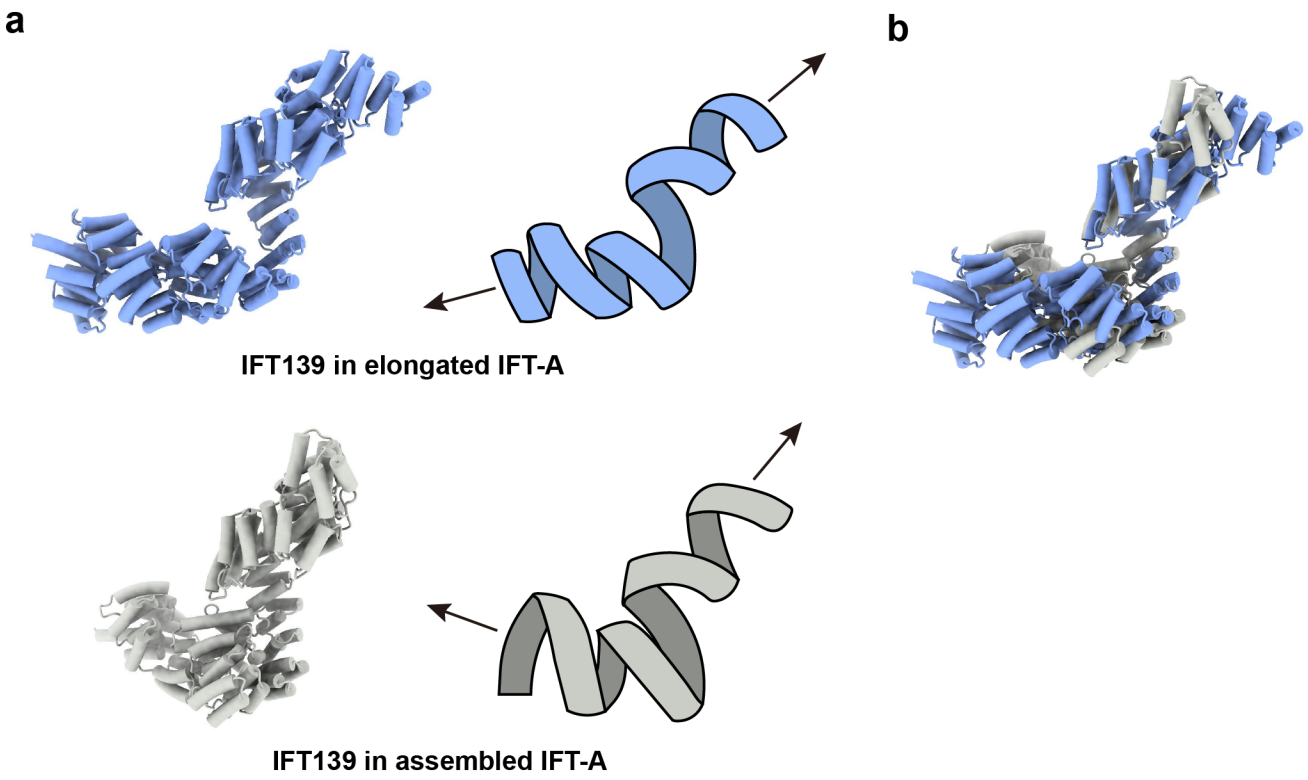

Supplementary Fig. 10 | Twist in IFT139$_N$ during the incorporation of the elongated IFT-A complex into the anterograde train. a, Cartoons and schematic diagrams showing the difference between solenoid structures of IFT139$_N$ in elongated state (light blue) and assembled state (gray) of the IFT-A complex. **b,** IFT139$_N$ is superimposed to compare the conformational changes in the two states in **(a)**.

Supplementary Fig. 11

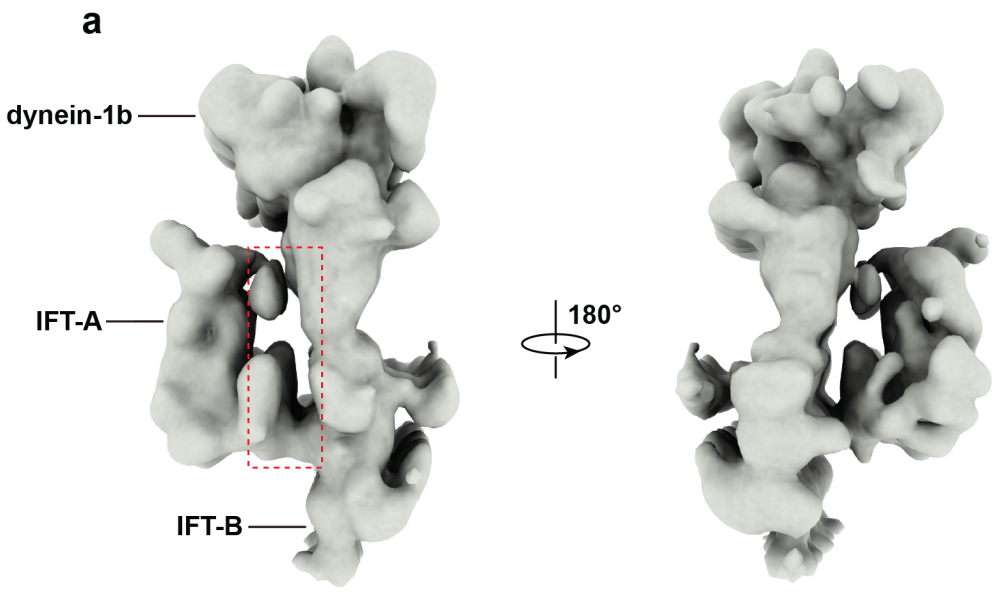

IFT-A/IFT-B train at 29.9 Å
(van den Hoek *et al.*)

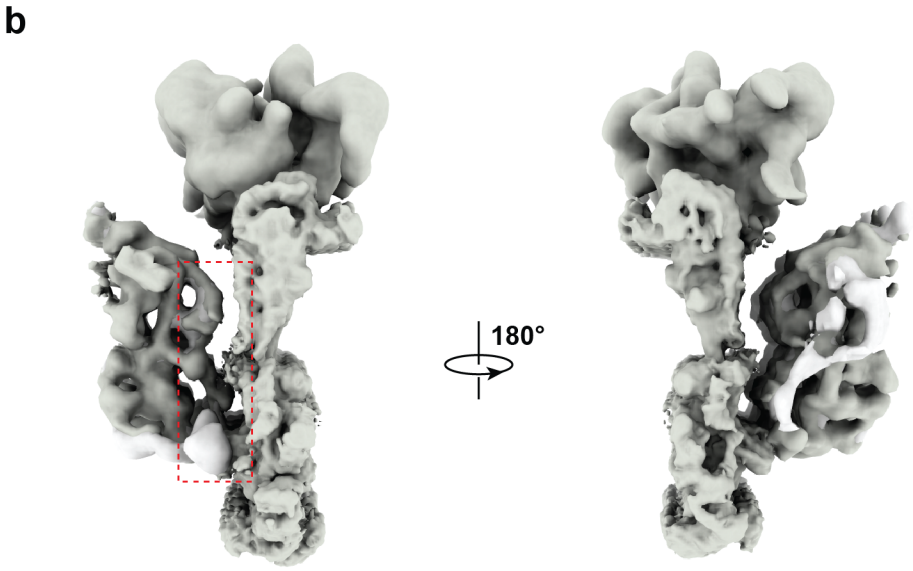

IFT-A (at 20.7 Å) / IFT-B train (at 9.9 Å)
(Lacey *et al.*)

Supplementary Fig. 11 | Interface between IFT-A and IFT-B in the anterograde train. **a,** Low-resolution *Chlamydomonas* IFT train map (EMD-15261) at the ciliary transition zone. **b,** Composite map generated by fitting high-resolution structures of IFT-A and IFT-B (EMD-15980 and EMD-15977) into the anterograde IFT train map in (a). Dashed rectangles denote the interfaces between IFT-A and IFT-B.

Supplementary Fig. 12

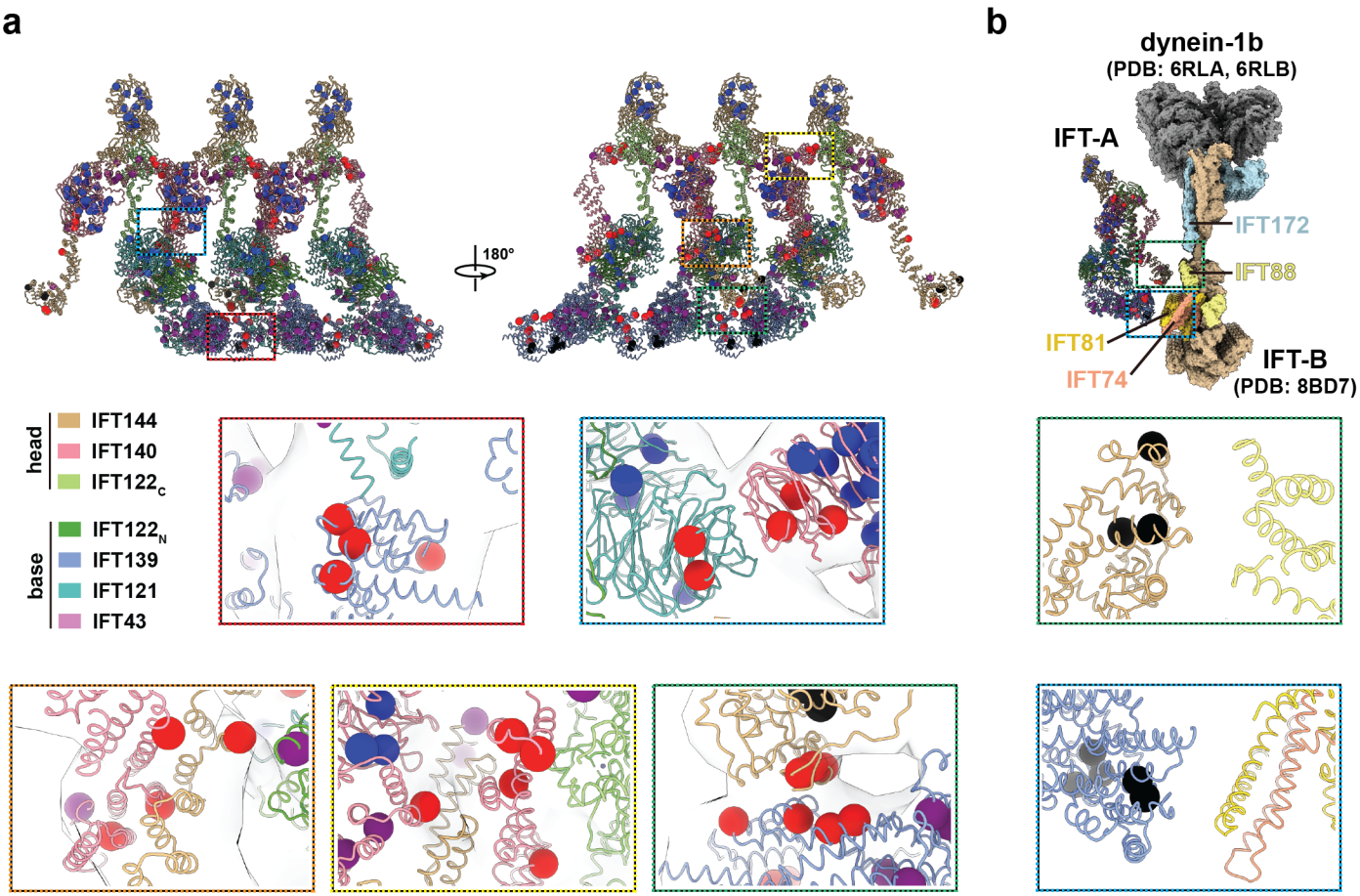

Supplementary Fig. 12 | Enlarged views of mutations at type-II and -III interfaces. **a,** Human disease mutations are mapped onto the assembled IFT-A of anterograde trains. Dashed boxes in colors indicate type-II mutations and closeup views of those mutations at the interfaces are shown below. **b**, The [IFT-A]-[IFT-B] interfaces. Closeup views of the type-III mutations at the [IFT-A]-[IFT-B] interfaces are shown below. Mutations of type I-IV are shown in blue, red, black and purple dots, respectively.